CHARACTERIZATION OF METAL ARTIFACTS IN DIFFUSION TENSOR IMAGING FOR SPINAL CORD APPLICATIONS

A Dissertation
Submitted to
the Temple University Graduate Board

In Partial Fulfillment
of the Requirements for the Degree
Master of Science in Mechanical Engineering

---

by
Devon M. Middleton
January, 2013

Examining Committee Members:

Feroze B. Mohamed, PhD, Department of Radiology, Department of Electrical Engineering

Nancy Pleshko, PhD, Department of Bioengineering

Scott H. Faro, MD, Department of Radiology, Department of Electrical Engineering

ABSTRACT

Diffusion Tensor Imaging (DTI) is a magnetic resonance imaging (MRI) technique used to measure in-vivo anisotropic water diffusion. This can give useful information regarding white matter integrity and has the potential to provide important biomarkers in spinal cord injury. One of the largest challenges in DTI of the spinal cord is the presence of metal which causes geometric distortions, signal pile-up, and signal voids. Because most patients with spinal cord injury have some amount of metal hardware implanted for stabilization, it is important to confront issues involving metal as DTI of the spinal cord becomes more widely examined. This study examined the characteristics of metal artifact in DTI images for several spinal surgical implants via imaging of phantoms constructed with implements suspended in agar gel to provide a homogeneous surrounding medium for analysis. A cervical spine phantom implanted with pedicle screws was also used to simulate in-vivo imaging. Optimization of the DTI sequence was also considered using different metal artifact reduction techniques including view-angle-tilting, slice thickness, and field of view size. Minor reduction in metal artifact was achieved using these techniques. The resulting image data shows that imaging near metal may be feasible in some circumstances, particularly when implantation is minimal. Also, using the cervical spine phantom it was shown that it should be possible to acquire DTI data close to the location of metal implants and thus examine DTI values of the injured spinal cord superior to the injury site.

TABLE OF CONTENTS

LIST OF TABLES

LIST OF FIGURES

CHAPTER 1

THEORY, METHODS, AND MATERIALS

Theory and Background

Introduction

Diffusion Tensor Imaging (DTI) is an effective technique in magnetic resonance imaging (MRI) for measuring anisotropic water diffusion in-vivo which can reveal useful information regarding the tissue microstructure, particularly in highly anisotropic structures such as white matter (1). Using DTI, white matter characteristics of the brain are being studied extensively and recently study of the spinal cord has become increasingly popular. In DTI of the spinal cord, the proximity of metal implants ubiquitous in patients with spinal cord injuries can make cord imaging extremely challenging. The presence of metal implants presents one of the largest challenges in MRI, causing distortion, signal loss, heating, and other physical threats (2). Even when MRI safe metals such as titanium are used as surgical implants, signal loss (at the location of the metal itself) and distortion (at metal-tissue interfaces) are present (3). These distortions can cause uncertainty in quantitative imaging methods when metal is present near areas of interest. As DTI of the spinal cord becomes more widely explored, it is important to examine the feasibility of imaging patients with implants, as well as to better understand the nature of the distortions and their impact on the image data.

Diffusion imaging and tensor estimation

The quantification of diffusion via spin echo measurements in the presence of a magnetic gradient has been well established since the 1960's in NMR spectroscopy. The principle of diffusion measurement is based on the MRI signal intensities of an echo received with no applied gradient, and an echo with pulsed magnetic gradients. In 1965, Stejskal and Tanner first derived an equation to relate these intensities to the self-diffusion coefficient (4). The Stejskal Tanner equation,

$$\ln[A(2\tau)/A(0)] = -\gamma^2 D\delta^2(\Delta - \tfrac{1}{3}\delta)g^2 \qquad (1)$$

has served as the basis for the vast majority of work on MR diffusion imaging. In this equation, $A(2\tau)/A(0)$ represents the ratio amplitude at the echo time to that at the excitation time, γ is the gyromagnetic ratio, g is the gradient amplitude, and δ is applied time of the gradient. The methodology for diffusion imaging using pulsed gradients can be effectively illustrated considering a one dimensional case where diffusion is purely isotropic, allowing the specific orientation of gradients to be ignored. In the presence of a static magnetic field, a 90 degree RF pulse is applied causing protons to begin to precess at a frequency ω, as in conventional MRI. A magnetic gradient is then applied along the diffusion axis resulting in an increase in all protons' precession frequencies based on position, since precession frequency is dependent on magnetic field strength. The gradient is then turned off and all protons return to the same precession frequency, ω, in the static field, however, the phase will differ by position as the precession of protons toward the higher strength end of the gradient will have precessed ahead of those toward the lower end. The practical result is that protons are "labeled" by their phase. A 180

degree refocusing pulse is then applied as in a normal spin echo measurement, and between the 180 degree pulse and the echo a second gradient is then applied, cancelling the first (Figure 1). If no protons move during this process, i.e. no diffusion occurs, the gradients will have no net effect, all protons in a given region will be in phase, and the echo generated will be identical to the echo with no diffusion gradients applied. However, if random diffusion occurs, the gradients will not cancel, protons in a given region will have not be in phase, and the echo intensity will be lower as compared to the echo from an unweighted image. So it can be said that diffusion weighted imaging measures diffusion by measuring signal decrease from an unweighted image to a weighted image.

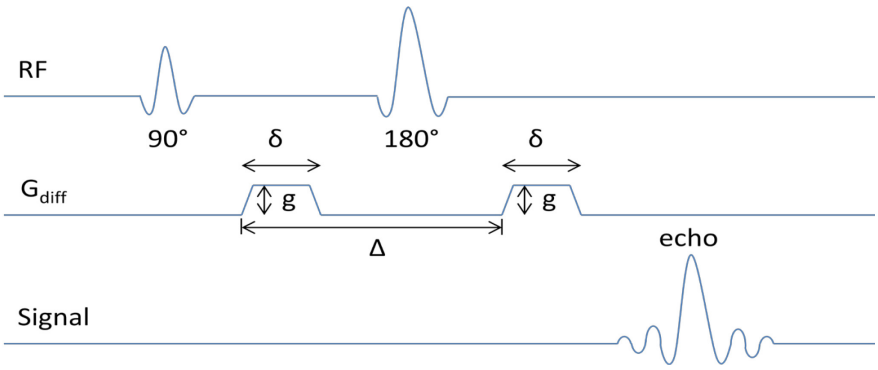

Figure 1 – Basic pulse sequence for one dimensional diffusion measurement.

DTI is an extension of this principle to anisotropic diffusion in three dimensions. Basser et al. used the relationship of the effective diffusion tensor, $\mathbf{D}^{\mathbf{eff}}$, to diffusion **J** and the concentration gradient ∇C in a medium:

$$\begin{bmatrix} J_x \\ J_y \\ J_z \end{bmatrix} = - \begin{bmatrix} D_{xx}^{\text{eff}} & D_{xy}^{\text{eff}} & D_{xz}^{\text{eff}} \\ D_{yx}^{\text{eff}} & D_{yy}^{\text{eff}} & D_{yz}^{\text{eff}} \\ D_{zx}^{\text{eff}} & D_{zy}^{\text{eff}} & D_{zz}^{\text{eff}} \end{bmatrix} \begin{bmatrix} \frac{\partial C}{\partial x} \\ \frac{\partial C}{\partial y} \\ \frac{\partial C}{\partial z} \end{bmatrix} \tag{2}$$

to arrive at a relationship between the log-transformed ratio of diffusion weighted to unweighted signal intensities and $\mathbf{D}^{\mathbf{eff}}$ as:

$$\ln\left[\frac{A(0)}{A(\mathbf{n})}\right] = [b_{xx}D_{xx}^{\text{eff}} + b_{yy}D_{yy}^{\text{eff}} + b_{zz}D_{zz}^{\text{eff}} + (b_{xy} + b_{yx})D_{xy}^{\text{eff}} + (b_{xz} + b_{zx})D_{xz}^{\text{eff}} + (b_{yz} + b_{zy})D_{yz}^{\text{eff}}] \quad , \tag{3}$$

where $A(0)$ is the unweighted signal intensity, and $A(\mathbf{n})$ is diffusion weighted image signal intensity for gradient direction $\mathbf{n}(2)$. The b-matrix represented by b_{ij} is a symmetric 3 x 3 matrix which is calculated for each diffusion direction based on pulse shape, amplitude, and spatial orientation (5).

Since $\mathbf{D}^{\mathbf{eff}}$ is a 3 x 3 symmetric matrix, there are effectively six unknowns. Thus, a minimum of six diffusion weighted images must be acquired in non-coplanar directions to resolve the tensor. In order to facilitate rapid estimation of $\mathbf{D}^{\mathbf{eff}}$, a vectorized approach is often used:

$$\begin{bmatrix} X_1 \\ X_2 \\ X_3 \\ X_4 \\ X_5 \\ X_6 \end{bmatrix} = \begin{bmatrix} b_{xx}^1 & 2b_{xy}^1 & 2b_{xz}^1 & b_{yy}^1 & 2b_{yz}^1 & b_{zz}^1 \\ b_{xx}^2 & 2b_{xy}^2 & 2b_{xz}^2 & b_{yy}^2 & 2b_{yz}^2 & b_{zz}^2 \\ b_{xx}^3 & 2b_{xy}^3 & 2b_{xz}^3 & b_{yy}^3 & 2b_{yz}^3 & b_{zz}^3 \\ b_{xx}^4 & 2b_{xy}^4 & 2b_{xz}^4 & b_{yy}^4 & 2b_{yz}^4 & b_{zz}^4 \\ b_{xx}^5 & 2b_{xy}^5 & 2b_{xz}^5 & b_{yy}^5 & 2b_{yz}^5 & b_{zz}^5 \\ b_{xx}^6 & 2b_{xy}^6 & 2b_{xz}^6 & b_{yy}^6 & 2b_{yz}^6 & b_{zz}^6 \end{bmatrix} \begin{bmatrix} D_{xx}^{\text{eff}} \\ D_{xy}^{\text{eff}} \\ D_{xz}^{\text{eff}} \\ D_{yy}^{\text{eff}} \\ D_{yz}^{\text{eff}} \\ D_{zz}^{\text{eff}} \end{bmatrix} \tag{4}$$

where X_n is the log transformed ratio of unweighted to weighted signal intensity for gradient direction n, and b_{ij}^n is the ijth element of the b-matrix for gradient direction n (6). The simplest tensor estimation process is then to compute $\mathbf{D}^{\mathbf{eff}}$ based on $\mathbf{B}$ inverse:

$$\mathbf{D}^{\mathbf{eff}} = \mathbf{B}^{-1}\mathbf{X}, \tag{5}$$

or if **B** is not square due to acquiring more than six gradient directions a pseudoinverse can be used:

$$\mathbf{D^{eff}} = (\mathbf{B}^{\mathrm{T}}\mathbf{B})^{-1}\mathbf{B}^{\mathrm{T}}\mathbf{X}. \quad (6)$$

In practice, this tensor estimation is performed voxel-wise for each voxel in each slice in an MR image, i.e. a 10 slice image with a 64 x 64 matrix will result in 40960 tensor estimations.

Diffusion indices

Several useful diffusion indices can be calculated from the effective diffusion tensor which can provide useful information about the tissue being imaged. The tensor's eigenvalues (λ_1, λ_2, λ_3) are the foundation of these indices, as well as important metrics themselves. The primary eigenvalue, λ_1, is also referred to as the longitudinal (or axial) diffusivity ($\lambda_\parallel$), and gives the magnitude of diffusion along the axis defined by the primary (corresponding to λ_1) eigenvector. The average of the second and third eigenvalues (λ_2, λ_3) provides the radial diffusivity ($\lambda_\perp$) perpendicular to the primary eigenvector, and the average of all three eigenvalues is referred to as the Mean Diffusivity (MD). Fractional Anisotropy (FA) is one of the most frequently used indices in DTI, and it is calculated from the eigenvalues as:

$$FA = \sqrt{\frac{1}{2}}\frac{\sqrt{(\lambda_1-\lambda_2)^2+(\lambda_1-\lambda_3)^2+(\lambda_2-\lambda_3)^2}}{\sqrt{(\lambda_1^2+\lambda_2^2+\lambda_3^2)}} \quad (7)$$

FA is effectively a ratio from zero to one representing the extent to which a diffusion tensor is anisotropic, i.e. a FA value of zero represents complete isotropy and a

value of one represents complete anisotropy. In order to represent three dimensional anisotropy in a two dimensional image, color FA maps are frequently used. Color FA maps are generated by multiplying the FA value by the magnitudes of the x, y, and z components of the primary eigenvector to create the map's red, green, and blue intensities, respectively.

DTI Applications in neuroimaging

DTI has become an important tool in neuroimaging due to its ability to identify abnormalities in white matter tracts by measuring diffusion indices, particularly FA and MD (7,8). These measurements are useful because normal white matter tracts comprise myelinated axons whose lipid myelin sheathes restrict diffusion to directions along the axon. In injured or pathological tissue, the myelin sheath degenerates resulting in more isotropic diffusion (Figure 2) (9). Thus, voxels containing a greater number of damaged axons will exhibit lower FA values than those containing mostly intact axons. These changes can be detected in tissue that is identifiable as injured/pathological in structural MRI, as well as normal appearing tissue (7).

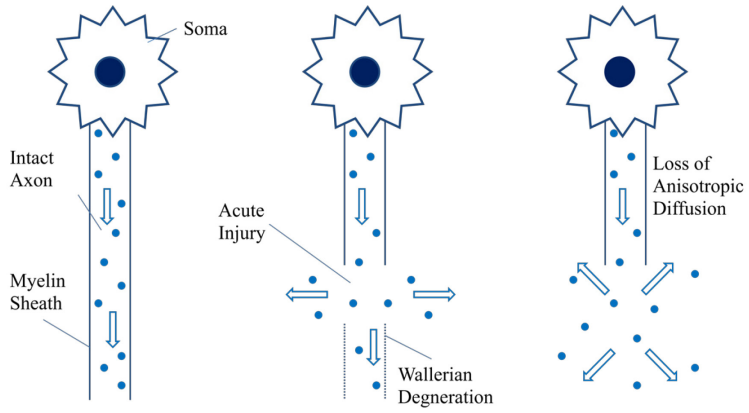

Figure 2 – Illustration of loss of anisotropic diffusion in a damaged axon

DTI of the spinal cord

Spinal cord DTI is an expanding area in MR research, including evaluation of acute injury and degenerative conditions (10-16). The spinal cord lends itself well to DTI due to the fact that it is an inherently anisotropic structure, largely comprising long, myelinated axons. Acquiring high-quality undistorted diffusion weighted images of the normal and injured/diseased spinal cord has the potential to aid in diagnosis and treatment, but several technical challenges exist in the acquisition of noise-free images.

A major difficulty is the impact of motion, which can result from patient movement, cord pulsation and oscillation, and respiratory motion (17-19). Quantitatively, motion can cause artifacts which can potentially result in overestimation of diffusion (13), and can also result in poor delineation between the spinal cord and surrounding cerebrospinal fluid. Cardiac and respiratory gating can be used to reduce motion artifacts during acquisition, but these methods extend scan time which in turn can lead to patient discomfort. Post-processing motion correction can be an effective means of improving image quality without increased scanning time (20).

Also as a consequence of motion, most DTI techniques employ echo planar imaging (EPI), which uses rapidly switching readout gradients to acquire a complete 2D image in a single repetition time (21). This rapid acquisition technique is helpful in reducing motion artifacts, but is subject to geometric distortions. In spinal cord DTI, the use of inner-field-of-view techniques which reduce phase FOV size have been shown to be effective in reducing distortion (11,16).

In practical imaging of the injured spinal cord, the greatest challenge will be the presence of metal in injured subjects. The majority of injured subjects will have some form of metal fixation hardware, including rods, pedicle screws, wires, cages, and hooks. The need to image in the presence of this metal is critical in the collection and analysis of spinal cord DTI data. Follow up of patients undergoing therapy, longitudinal studies to understand the progression of the cord characteristics between acute and chronic states becomes difficult with a metal hardware present around the spinal cord area.

Magnetic susceptibility

Magnetic susceptibility is the magnitude of a material's reaction to a magnetic field, where the material's magnetization M is equal to the susceptibility χ multiplied by the applied field strength B_0 (22). This property is responsible for the difficulties in MR imaging near metal implants since metals have much higher susceptibilities as compared to body tissues as shown in Table 1.

Table 1 – Magnetic susceptibilities of tissues and common implant metals (22)

Material	**χ(ppm)**
Tissue/bone	-10
Air	0.3
Titanium	178
Cobalt-Chromium	900
Stainless Steel	3000-5000

As is clear, even the least susceptible metal used in MR safe implants result in a much greater susceptibility difference from tissue than air, and the air-tissue interface at χ = ~10 ppm is already capable of producing noticeable susceptibility artifacts.

Metal artifacts in MRI

Susceptibility artifacts occur due to a difference in magnetic susceptibilities between two adjacent materials. Considering a cylinder of susceptibility χ_1 suspended in a medium of susceptibility χ_2, the inside of the cylinder is subject to an magnetic field of strength $\frac{1}{2}(\chi_1 - \chi_2)B_0$ in addition to the static field B_0 and a dipole magnetic field will be created in the medium outside the cylinder resulting in shape distortions and intensity increases(23). As is shown by the preceding equation, the severity of susceptibility artifacts is dependent on the relative susceptibilities of adjacent materials, and the strength of the applied magnetic field. An unfortunate consequence of this is the fact that higher field strengths are preferable in achieving higher resolutions and signal-to-noise ratio (SNR), and susceptibility artifacts will increase as well. Other artifacts can be non-susceptibility related, including eddy currents which are induced currents in conductive materials exposed to changing magnetic fields in accordance with Faraday's law. Eddy currents are always present to some extent in MRI due to conducting elements such as coils and other metal structural components (24), but are much more severe in the case of metal in the imaging volume which is not shielded or otherwise compensated for. The effects of eddy currents on MR images include resolution degradation, misregistration, decreased SNR, and proton phase change(25).

Reducing metal artifacts

Several techniques exist for reducing distortions when imaging near metal implants in MRI. One technique is pre-polarization, which relies on a pre-polarizing pulse and a subsequent readout field which is much lower in strength than conventional

MR static fields (26). Pre-polarization has been shown to be effective in reducing metal artifacts as compared to conventional MRI, but implementation requires specialized hardware (27). This makes the technique less than ideal, since it cannot be easily implemented on the existing installed base of MR scanners.

View-angle-tilting (VAT) is another technique which can be used to correct metal artifacts. VAT utilizes a compensation gradient equal in amplitude to the slice selection gradient during readout at an orientation which tilts the viewing angle and can correct for shifts resulting from field inhomogeneity (28). In other words, the readout direction is tilted to allow the slice to be viewed at an angle which compensates for in-plane chemical shifts. This technique has been implemented in structural imaging as the metal artifact reduction sequence (MARS), and has been shown to effectively reduce distortions albeit at some cost to SNR (29).

An extension of VAT which includes additional z-phase encoding has recently been developed and has shown promise in imaging near metal artifacts (30). This technique, Slice Encoding for Metal Artifact Reduction (SEMAC), is effective in reducing in-plane and through-plane artifacts, and is capable of acquiring structural images in a feasible amount of time (31,32). Through-plane artifacts result from distortions in the slice excitation profile due to local inhomogeneity caused by metal which cause excitation in spins outside the desired slice and failure to excite spins within the slice. SEMAC corrects for this by using additional phase encoding around the selected slice to reassign excited spins to the correct slice during reconstruction.

While all of these techniques have demonstrated efficacy in reducing metal artifacts in structural imaging, their usefulness in diffusion applications remains unexamined. Certainly, some of the drawbacks inherent in these techniques – increased scan time, reduced SNR – are in conflict with the requirements for DTI. However, some inclusion of these concepts may prove useful in sequence optimization for DTI near metal implants.

Methods and Materials

Surgical implant rod phantoms

Samples of rods used clinically for spinal stabilization were acquired from Shriners Hospital. The samples comprised three 5.5mm diameter rods made of stainless steel, cobalt-chromium, and titanium, with an additional 3.5mm titanium rod for a total of four. All rods were ensured to be safe for MRI prior to scanning. Initial test phantoms were constructed by suspending the rods in gelatin; however the lack of stability of the gelatin proved problematic. Phantoms were then constructed by suspending the rods horizontally in a 2% agar gel which provided substantially greater stability.

Imaging

Phantoms were imaged initially using three sequences: a standard full FoV EPI diffusion sequence, a newly developed iFoV EPI diffusion sequence, and a T2 weighted spin-echo sequence (a structural imaging sequence). Sequence parameters are given in Table 2. Both diffusion sequences were acquired with 20 gradient directions, two averages, and a b-value of 1000 s/mm^2.

Table 2 – Sequence parameters

Sequence	TE (ms)	TR (ms)	FoV Width (mm)	Phase FoV	Voxel Height (mm)	Voxel Width (mm)	Slice thickness (mm)
T2	90	3630	200	100%	0.8	0.6	3.0
Full FoV	93	6200	220	100%	1.7	1.7	3.0
iFoV	89	6600	250	17.3%	1.2	1.2	3.0

Slices were acquired axially with the rods positioned parallel to the scanner's z-axis. Figure 3 shows representative axial slices for each sequence.

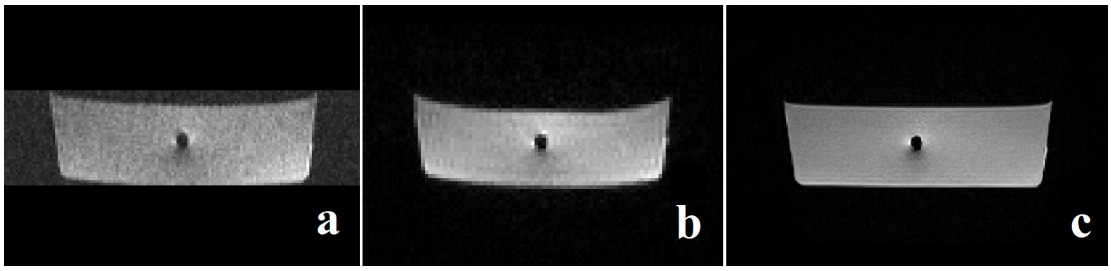

Figure 3 – Axial slices acquired with iFoV sequence (a), full FoV sequence (b), and T2 spin-echo sequence (c)

Analysis software

Custom analysis software was developed using Matlab (The Mathworks, Natick, MA, USA). The software allows viewing and analysis of image series in DICOM format as provided by the Verio 3T scanner by collecting header data, sorting and organizing series, and loading image data for viewing. All code was developed in house, as it is critical to have a fully flexible and expandable tool for analysis as new needs arise during investigation. Several analyses can be performed using the software. In the case of diffusion series, tensor estimation based on diffusion weighted images is possible and image maps for common indices, including eigenvalues, MD, FA, and color FA (Figure

4). Additionally, region-of-interest (RoI) based analysis is implemented, allowing for DTI index calculation for regions specified by circle, rectangle, or free-form polygon.

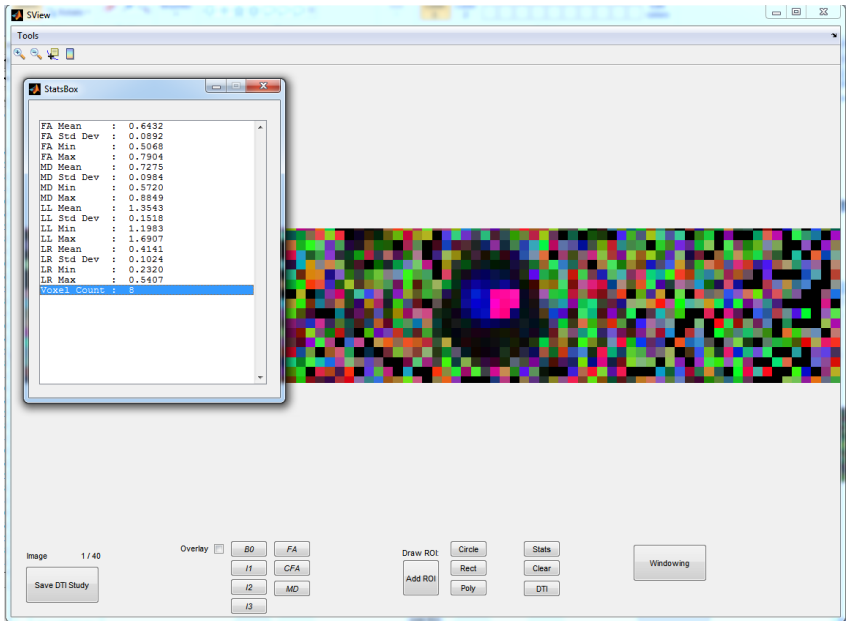

Figure 4 – Screenshot of analysis software showing color FA map and calculated DTI indices for a RoI (highlighted in red)

Impact radius estimation

Functionality specific to metal artifact examination was also developed for the analysis software. The impact radius of artifacts present is estimated based on examining expanding concentric annular RoIs from the center of the metal rod. Mean intensity and standard deviation are calculated for each region and when the RoI meets criteria for homogeneity, the edge of the impacted region can be defined. The RoI is considered to have returned to homogeneous when its mean intensity varies by less than 10% from the previous RoI and its standard deviation is less than a specified fraction of its mean intensity. This fraction is determined by an examination of the region surrounding the

rod. Using the analysis software, RoIs were drawn to include the homogeneous region of the phantom, i.e. the region not affected by metal artifact or effects at the phantom edge.

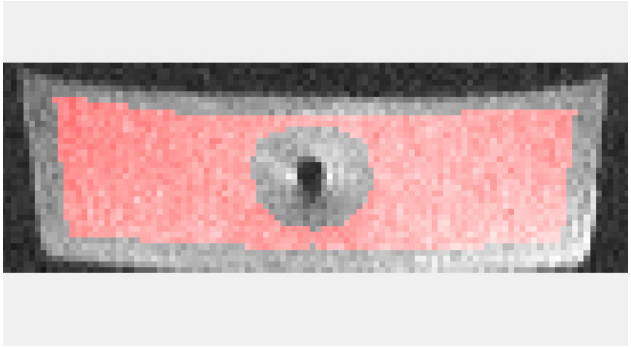

Figure 5 – Representative RoI (shown in red) used to measure intensity and standard deviation of homogeneous regions.

Each RoI was thus drawn to conservatively to avoid artifact; Figure 5 shows a representative RoI. The mean intensity and standard deviation for the RoI were calculated in order to determine the appropriate criteria for standard deviation as a fraction of mean intensity (standard deviation tolerance). Measurements were performed on five slices for each rod and for both diffusion sequences (full FoV and iFoV).

CHAPTER 2

PRELIMINARY IMAGING AND SEQUENCE OPTIMIZATION

Preliminary Scans of Surgical Implant Rods

Homogeneity criteria estimation

All rod phantoms were imaged using both the iFoV and full FoV sequences. After intensity and standard deviations were measured slice-by-slice for each rod/sequence combination, averages for all slices were calculated (Table 3). Complete measurement data for all slices is given in Appendix A. The ratio of standard deviation to mean intensity was noticeably lower for the full FoV sequence in the case of the titanium phantoms indicating better homogeneity, but the ratio was comparable to the iFoV sequence for the cobalt-chromium phantom. The averaged ratio of standard deviation to mean intensity was rounded up to the nearest 0.05 when defining criteria for impact radius estimation as an attempt to ensure convergence.

Table 3 – Summary of measurements for homogeneous regions

Material	Sequence	Averaged Mean Intensity	Averaged Std.Dev	Averaged Std.Dev/ Mean	Min Std.Dev/ Mean	Max Std.Dev/ Mean
Ti 3.5mm	iFoV	270	32	0.117	0.113	0.121
	full FoV	413	35	0.085	0.077	0.092
Ti 5.5mm	iFoV	257	32	0.124	0.117	0.130
	full FoV	395	32	0.082	0.076	0.085
CoCr 5.5mm	iFoV	269	30	0.113	0.107	0.124
	full FoV	403	48	0.119	0.110	0.136

Stainless steel is not included in Table 3 due to the fact that the images were too distorted to effectively measure the homogeneous region (Figure 6). These results were not altogether surprising since the magnetic susceptibility of stainless steel is 3-5 times the susceptibility of cobalt-chromium and 17-28 times that of titanium as shown previously in Table 2. The severity of the stainless steel artifacts unfortunately eliminated the material for consideration.

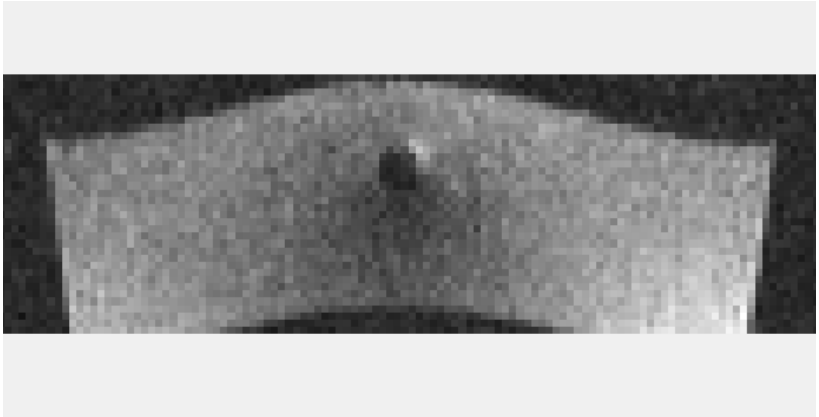

Figure 6 – Axial slice showing severe distortions, both intensity and geometric, from the 5.5mm stainless steel rod. Other slices acquired for the stainless steel rod phantom were comparable or worse in quality.

Impact radius estimation

The impact radius of artifact was estimated for the 5.5mm titanium, 3.5mm titanium, and 5.5mm cobalt-chromium rods. Estimation was performed as described previously on five slices from the averaged b0 image for each diffusion sequence, and the slices selected were the same as those used in measurements for homogeneous regions given in the methods section. Visual inspection was used as an initial assessment of all estimated impact radius estimates (illustrated in Figure 7) and showed that all estimates appeared to effectively exclude regions containing artifact.

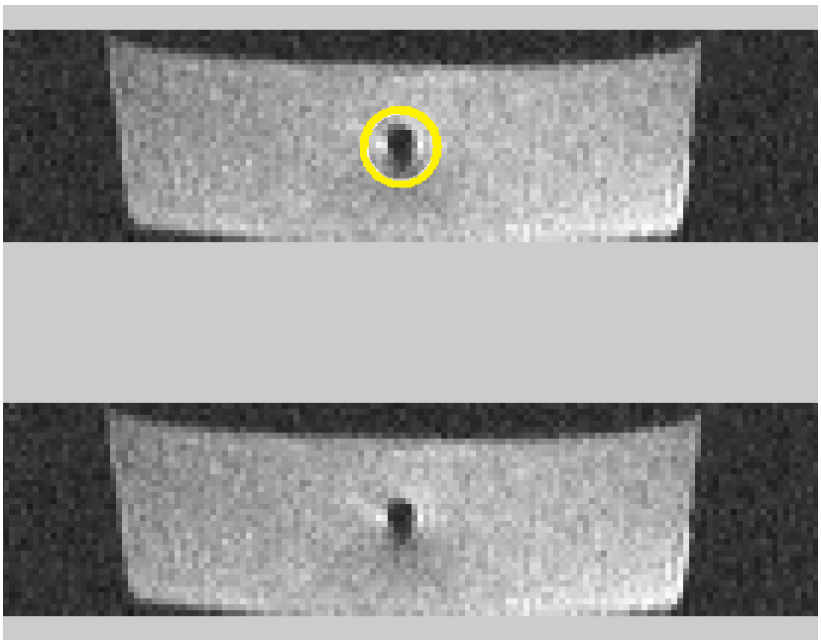

Figure 7 – Results from impact radius estimation for the purpose of visual inspection showing the original image (bottom) and the image with the radius of impact super-imposed (top). The yellow circle indicates the annular RoI which is considered to have returned to homogeneity. Intensity artifacts on the right and left sides of the rod are clearly contained within the inner radius.

The estimated impact radius for all materials and sequences ranged from 5.1mm to 9.3mm, with an average of 7.0mm. Table 4 summarizes the results of the estimations; complete data is given in Appendix A. Standard deviation tolerances as determined by the methods described were effective in obtaining convergent estimates in all cases except for the full FoV sequence for the 5.5mm cobalt-chromium rod. In this case, the standard deviation tolerance was increased by 0.01 and estimation was performed, repeating until a convergent impact radius was found.

Table 4 – Summary of impact radius estimations

Rod	FoV Size	Std. Dev. Tolerance Criteria	Average Impact Radius (mm)	Min Impact Radius (mm)	Max Impact Radius (mm)	Std. Dev. (mm)	Average Impact Radius/ Diameter
Ti 3.5mm	iFoV	0.15	5.5	5.1	5.7	0.3	1.56
	full FoV	0.10	6.4	6.0	6.6	0.3	1.82
Ti 5.5mm	iFoV	0.15	7.7	6.9	8.4	0.7	1.41
	full FoV	0.10	6.9	6.3	7.2	0.4	1.25
CoCr 5.5mm	iFoV	0.15	7.9	6.6	9.3	1.2	1.43
	full FoV	0.18-0.20	7.4	6.0	8.7	1.0	1.35

The ratio of average impact radius to rod diameter (RIRRD) was relatively consistent across materials for each sequence, with some important caveats. In general, the full FoV sequence resulted in lower RIRRD than did the iFoV sequence. However, in the case of the 3.5mm rod, the full FoV sequence resulted in a nearly 50% increase in the RIRRD, greater than that of the iFoV sequence for the same phantom. This is likely due to the decreased resolution of the full FoV sequence which does not resolve smaller artifacts as effectively and thus averages them into a larger region; i.e. the decrease in resolution of the full FoV sequence results in a larger artifact for small objects. This also suggests that the full FoV sequence may give better convergence in larger diameter rods due to higher SNR and improved image homogeneity resulting from the larger voxel size. This would make the iFoV sequence more appealing as a candidate for use in imaging near metal. In the case of the cobalt-chromium phantom, the impact radius could not be estimated until the standard deviation tolerance was increased substantially. Visual inspection of the images for both sequences revealed increased intensity artifact and geometric distortion in the full FoV image (Figure 8). The homogeneous regions in the full FoV sequence appeared more homogeneous than those in the iFoV sequence.

However, the iFoV sequence decreased both intensity artifacts and geometric distortions, resulting in comparable impact radius at stricter tolerances.

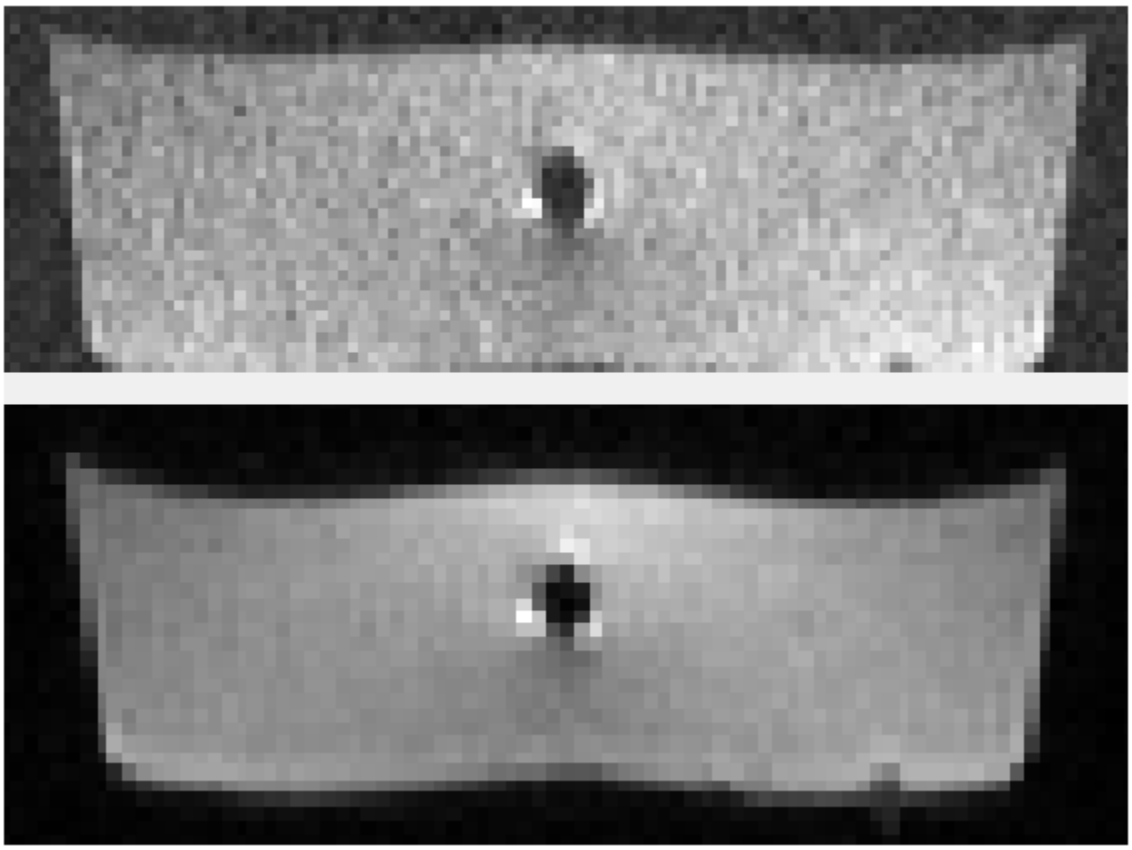

Figure 8 – b0 images of the cobalt-chromium phantom for the full FoV (bottom) and iFoV (top) sequences. Decreases in artifact are apparent in the iFoV image.

Sequence Optimization

As discussed previously, several methods for decreasing metal artifacts exist including pre-polarization, VAT, and additional z-phase encoding. Additionally, voxel volume, FoV size, and receiver bandwidth can impact metal artifacts (33). Of the first three techniques, only VAT was available as it was already implemented in the iFOV

sequence used. Voxel volume (via variation of slice thickness) and FoV size were also reasonably easily varied to allow for testing of artifact reduction. Receiver bandwidth was necessarily high due to the shorter TE used and difficult to vary without impact other parameters in the sequence. Initial optimization was performed using rod phantoms and parameters slice thickness, FoV size, and VAT. Optimization was only performed for the iFOV sequence due to the fact that it has been shown to be more effective in imaging of the pediatric spinal cord and our ultimate goal was to image the pediatric SCI population with spinal stabilization hardware present. The 5.5 mm titanium rod phantom was selected for optimization as titanium implants are most common and the best candidates for imaging due to lower magnetic susceptibility.

Slice Thickness

Reduction in slice thickness is capable of improving through plane artifacts resulting from metal, but results in reduced signal due to a decrease in voxel size. The rod phantom was imaged axially using 1 mm, 2 mm, and 3 mm (base sequence) slice thickness using the iFOV sequence and signal measurements were taken on a selected slice midway along the rod. The decrease in SNR was greater than 50% from 3 mm to 2 mm and at 1 mm the SNR was nearly identical to the ratio of the signal to its own standard deviation (Figure 9). The result was decreases in both SNR and image quality that were too severe to compensate for even if useful reduction in metal artifact were found (Figure 10).

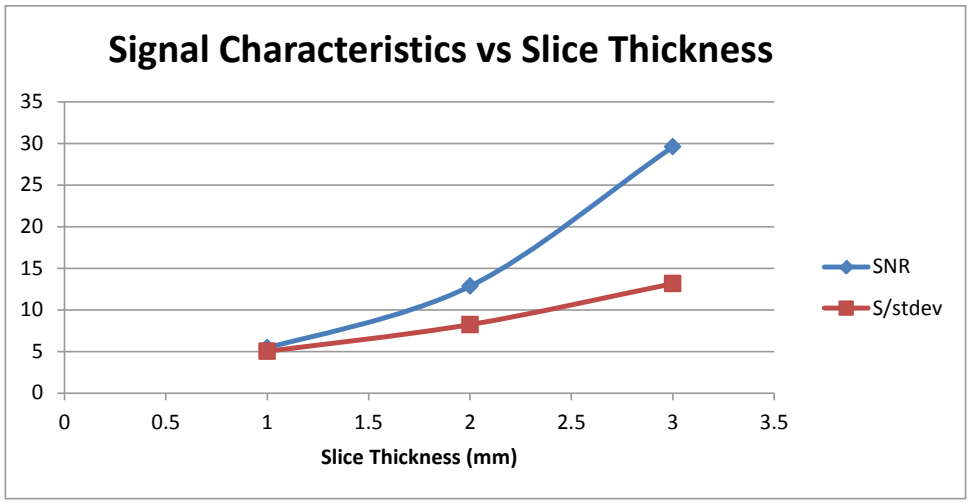

Figure 9 – Signal Characteristics by slice thickness for images acquired using the iFOV sequence.

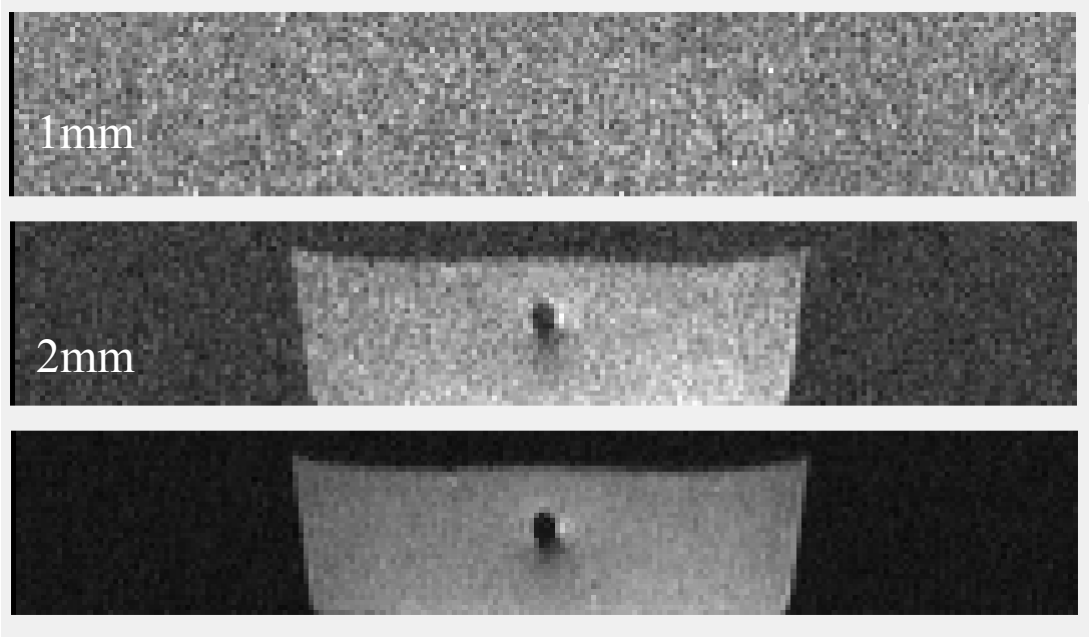

Figure 10 – Images acquired at 1 mm, 2 mm, and 3 mm slice thicknesses. Decrease in SNR is readily apparent at 2 and 1 mm.

FoV Size

Reduction in FoV size can result in a decrease in in-plane metal artifact without impacting SNR, provided the FoV is still sufficient to image the desired anatomy.

Because the sequence being optimized was an iFOV sequence with a smaller phase FoV already, the reduction in FoV size was accomplished by decreasing the frequency FoV and adjusting the phase FoV percentage in order to maintain a constant phase FoV size. FoV sizes of 250mm (base sequence), 230mm, 200mm, and 180mm were examined for improvement in metal artifact. Again, the 5.5mm titanium rod phantom was imaged using 3mm axial slices. The impact radius was then estimated for five representative slices at the approximate center of the rod (Table 5). Representative slices were chosen at the center of the rod where distortion characteristics were consistent from slice to slice.

Table 5 – Impact radius by FoV size for 5.5mm titanium rod, five representative slices

FOV	Slice	Impact Radius (mm)	% diff
250 mm	1	6.3	
	2	6.9	
	3	6.9	
	4	7.2	
	5	6.6	
230 mm	1	6.6	5%
	2	6.6	-4%
	3	6.9	0%
	4	6.6	-8%
	5	6.3	-5%
200 mm	1	6.9	10%
	2	6.6	-4%
	3	6.6	-4%
	4	6.9	-4%
	5	6.6	0%
180 mm	1	6.3	0%
	2	6.6	-4%
	3	6.6	-4%
	4	6.6	-8%
	5	6.6	0%

In general, some small amount of reduction in impact radius was found with reduced FoV size. Decreases in average impact radius as compared to the base sequence ranged from 0.1mm to 0.3mm, and by percentage the decreases were 2.7%, 0.9%, and 3.5% for the 230mm, 200mm, and 180mm sequences, respectively. While decreases were measureable, they remained minimal when compared to artifact size.

VAT

View angle tilting is a well established technique for reducing in-plane metal artifact and has been the most commonly used technique for this purpose. As described previously, VAT utilizes a compensation gradient equal off-angle to the slice selection gradient. This can result in image blurring at lower receiver bandwidths, but since the iFOV sequence employs a relatively high bandwidth this was not an issue.

As with reduced FoV testing, the 5.5mm titanium rod phantom was imaged axially. Tilt angles of 0° (base sequence), +5°, +10°, -5°, and -10° were employed. However, at angles greater than 5° in magnitude (+/-10°) images suffered from homogeneity issues manifested by a signal intensity gradient in the phase encoding direction rendering them unreliable for DTI analysis (Figure 11).

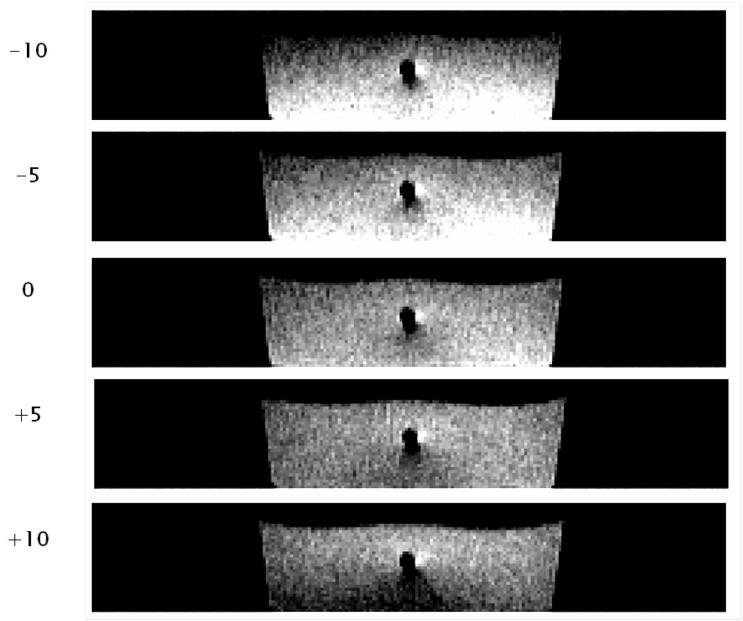

Figure 11 – Titanium rod phantom imaged at tilt angles from -10° to +10°. Images are contrast adjusted to illustrate the signal gradient introduced by VAT.

As with FoV size, measurements from five representative slices at rod center were taken to determine impact radius. Tilt angles of +/- 5° did result in substantive changes to the measured impact radius (Table 6). A tilt angle of +5° resulted in an average impact radius of 7.8 mm compared to 6.8 mm at 0°, a 15% increase. At a tilt angle of -5°, the average impact radius decreased by 9.7% from 0°, with an average of 6.1 mm.

In addition to the measured differences in impact radius, visual changes in the metal artifact region were observable in images acquired using different tilt angles. A dark region inferior to the rod was noticeably decreased at a tilt angle of -5°, and increased at +5° compared to the base sequence. These visual differences concur with the measurements given in Table 6. Figure 12 shows these differences on a representative slice.

Table 6 - Impact radius by tilt angle for 5.5mm titanium rod, five representative slices

Tilt Angle	Slice	Impact Rad	% diff
	1	6.3	
	2	6.9	
0 deg	3	6.9	
	4	7.2	
	5	6.6	
	1	8.4	33%
	2	7.2	4%
+5 deg	3	8.1	17%
	4	7.8	8%
	5	7.5	14%
	1	5.7	-10%
	2	6.3	-9%
-5 deg	3	6.3	-9%
	4	6.3	-13%
	5	6.0	-9%

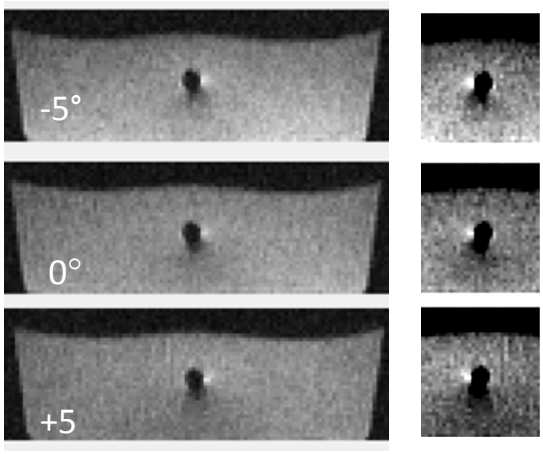

Figure 12 – 5.5 mm titanium rod phantom imaged with tilt angles of 0°, +5°, and -5°. A decrease in the dark region inferior to the rod center is observable at -5°, and an increase is observable at +5°. Images on right are zoomed and contrast adjusted to highlight changes in inferior region.

Of the artifact reduction techniques employed, VAT was the only method which produced substantive improvement. In addition, there were no major detriments to image quality or characteristics as exist with the other two methods (SNR loss, decreased imaging area). However, this was only true with relatively small tilt angles (+/- 5°) due to the fact that large tilt angles created homogeneity issues which compromised the quality of the imaged region beyond the area of metal artifact. While VAT has been used widely in structural imaging with conventional spin-echo or turbo/fast spin-echo sequences for the purpose of metal suppression, no reports were found of the use of VAT in EPI sequences for the purpose of metal artifact reduction. While relatively insensitive to motion, EPI sequences are inherently more prone to artifact and geometric distortions than spin-echo based sequences, and it cannot be assumed that expected improvements in artifact reduction for VAT EPI sequences should be consistent with improvements for VAT SE sequences. Thus, it is difficult to qualify the improvements found as being good or even useful without a larger context for discussion.

CHAPTER 3

SURGICAL IMPLANT IMAGING

After rod imaging, phantoms were constructed for imaging of additional surgical implements, including titanium pedicle screws and a titanium cage. Rods are used in conjunction with pedicle screws to create a stabilizing framework when vertebra are damaged or when spinal alignment is impacted by injury. Cages are used in spinal stabilization to provide structural support when the vertebral body is damaged. As with the rod phantoms, the surgical implements were suspended in a 2% agar gel to provide a homogeneous surrounding medium for examining artifact.

The first pedicle screw was a 4mm diameter titanium polyaxial screw with a total length of 66mm including the head. The second pedicle screw used was a 4mm diameter titanium polyaxial screw with a total length of 43mm including the head. The cage used was a 30mm long section of 14mm titanium mesh cage. Figure 13a shows both the 43mm screw and cage, and Figure 13b shows the complete agar phantom with suspended pedicle screw.

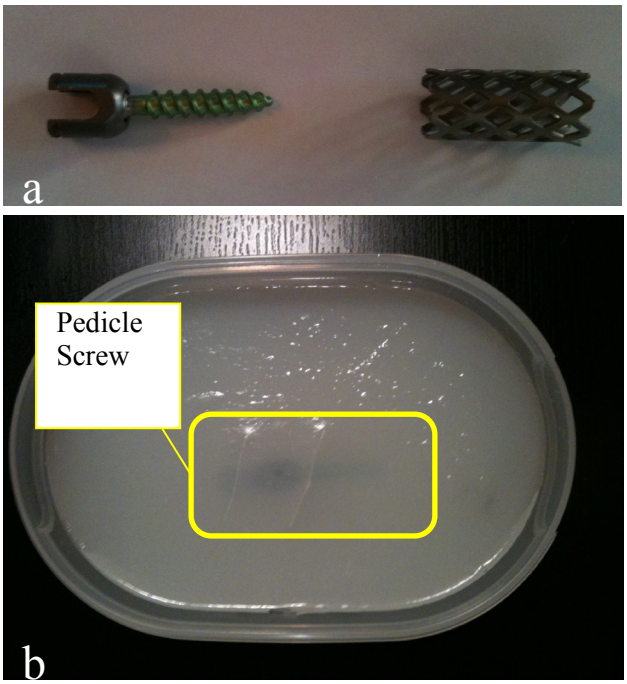

Figure 13 – Titanium screw, cage, and screw phantom. a: Titanium pedicle screw and titanium mesh cage used in implant phantom. b: complete phantom showing screw suspended in agar gel.

The surgical implant phantoms were imaged with the same iFoV base sequence used for the original rod phantoms with TE = 89ms, TR = 6600ms, voxel size = 1.2x1.2x3mm^3, b = 1000 s/mm^2, 20 diffusion directions, and 2 averages. The 66mm pedicle screw and cage were imaged axially with respect to the axis of the scanner bore. The 43mm pedicle screw was imaged in a sagittal orientation by rotating the phantom perpendicular to the bore axis; slices were acquired axially with respect to the scanner bore in all cases.

Metal artifacts were considerably more severe in the screw and cage phantoms. This was due to two major factors: increased size versus the original rod phantoms, and more complex shapes featuring more metal/gel interfaces. Since metal artifacts are

caused by differences in magnetic susceptibilities between adjacent materials, features like threads or meshing result in increased susceptibility artifact as compared to continuous interfaces. Distortion in the phase encoding direction was dominant, and extended beyond the physical confines of the phantoms. Because of this, changes were required in the methods for impact estimates. Rather than using concentric annular ROIs to estimate an impact radius, expanding rectangular ROIs were used from the distortion center to estimate an impact distance.

Axial Titanium Screw

The greatest distortion occurred at either end of the 66mm pedicle screw, and at the interface between the screw shaft and rotating head. The smallest distortion was along the shaft body. The estimated impact distance ranged from a minimum of 5.4mm to a maximum of 27.5mm, with an average of 15.7mm. The total length of the impact was 90mm (30 slices) and the total impacted area was 2833.7 mm^2. Figure 14 shows the estimated impact distance along the length of the screw superimposed on a midline coronal reconstruction from an axial turbo-spin-echo T2 weighted scan of the phantom. Slice-by-slice impact distance estimates are given in Appendix B.

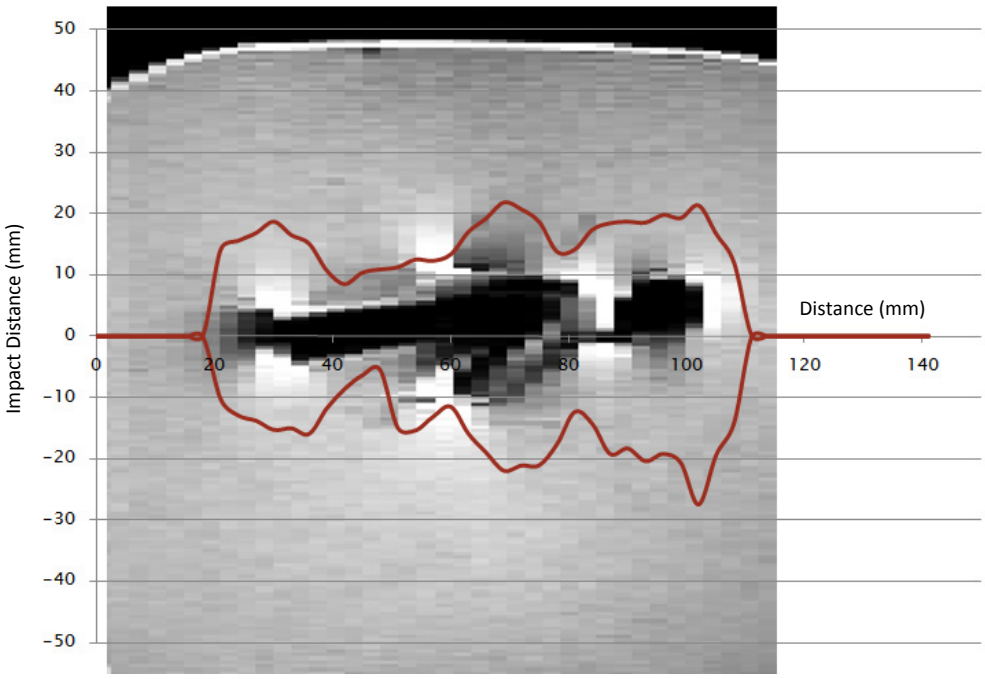

Figure 14 – Impact distance vs. distance (in mm) along 66mm pedicle screw axis superimposed over T2 TSE image of phantom. The y-axis shows impact distance from the centerline, and the x-axis gives the distance along the screw axis.

Sagittal Titanium Screw

The impact distance for the 43mm pedicle screw in a sagittal orientation ranged from 8.6mm to 40.0mm with an average of 23.6mm, and total impacted distance along the imaging axis was 72mm (24 slices). Despite being a smaller screw, imaging in the sagittal orientation resulted in considerably increased artifact as compared to axial orientation. The total impacted area 3680.6 mm^2, a 30% increase from the axially oriented screw. The estimated impact distance by slice along with the coronal T2 reconstruction are shown in Figure 15, and complete results are given in Appendix B.

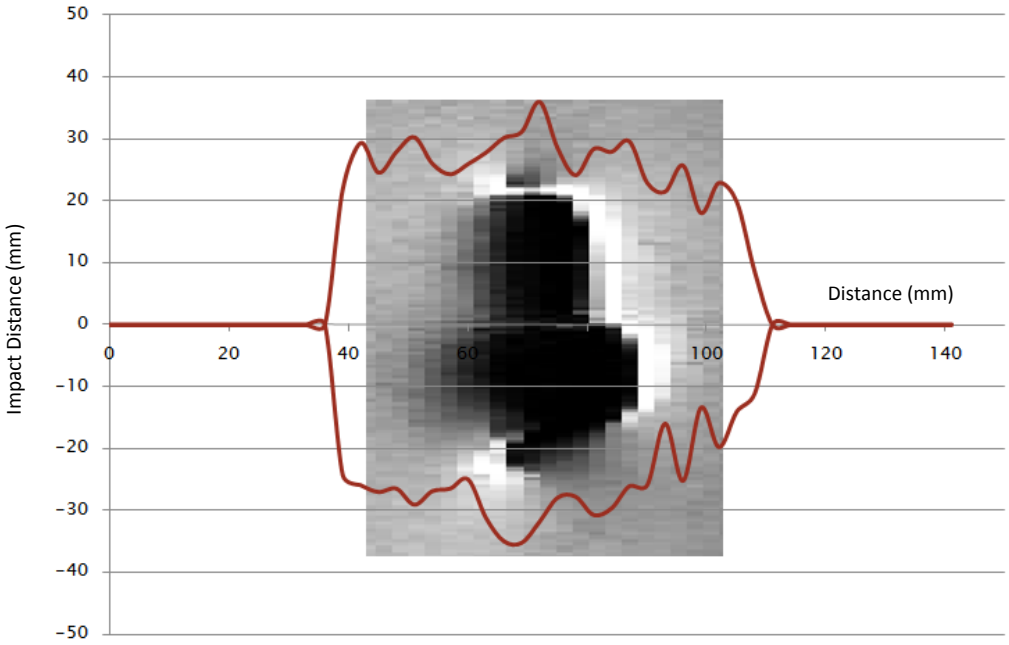

Figure 15 – Impact distance vs. distance (in mm) along 43mm pedicle screw axis superimposed over T2 TSE image of phantom.

Axial Titanium Mesh Cage

Impact distance along the metal cage was relatively consistent as would be expected given the relatively uniform geometry as compared to the pedicle screws. The minimum impact distance measured was 8.8mm, the maximum was 18.8mm, and the average was 12.2mm. The total impacted length was measured as 66mm (22 slices), and the total impacted area was 1609.2 mm^2. Figure 16 shows the impact distance along the cage axis, and complete measurements are shown in Appendix B.

Figure 16 – Impact distance vs. distance (in mm) along titanium mesh cage axis superimposed over T2 TSE image of phantom.

VAT for Axial Screw

Since VAT was the only substantively effective artifact reduction technique when imaging the titanium rod phantom, it was employed to determine whether improvements could be made in the more severe artifacts found when imaging implants. The 66mm titanium screw was again imaged axially using the same base sequence with tilt angles of +/-5°. Impact distance was again estimated slice-by-slice. As with the titanium rod phantom, a tilt angle of -5° decreased artifact size, and a tilt angle of +5° increased artifact (Table 7). However, the magnitude of increase/decrease was smaller in the case of the pedicle screw. At -5°, the average impact distance decreased by 4.9% for the pedicle screw as compared to 9.7% in the titanium rod, and at +5°, the average distance increased by 1.6% for the pedicle screw and 15.0% for the titanium rod. Figure 17 shows impact distance for tilt angles of 0°, +5°, and -5° along the pedicle screw axis.

Table 7 – Artifact impact measurements for 66mm titanium screw

	Impact Distance (mm)			Total Impacted
	Min	**Max**	**Avg**	**Area (mm^2)**
0 deg	5.4	27.5	15.7	2833.7
-5 deg	4.1	24.2	15.0	2700.6
+5 deg	6.8	32.6	16.0	2884.7

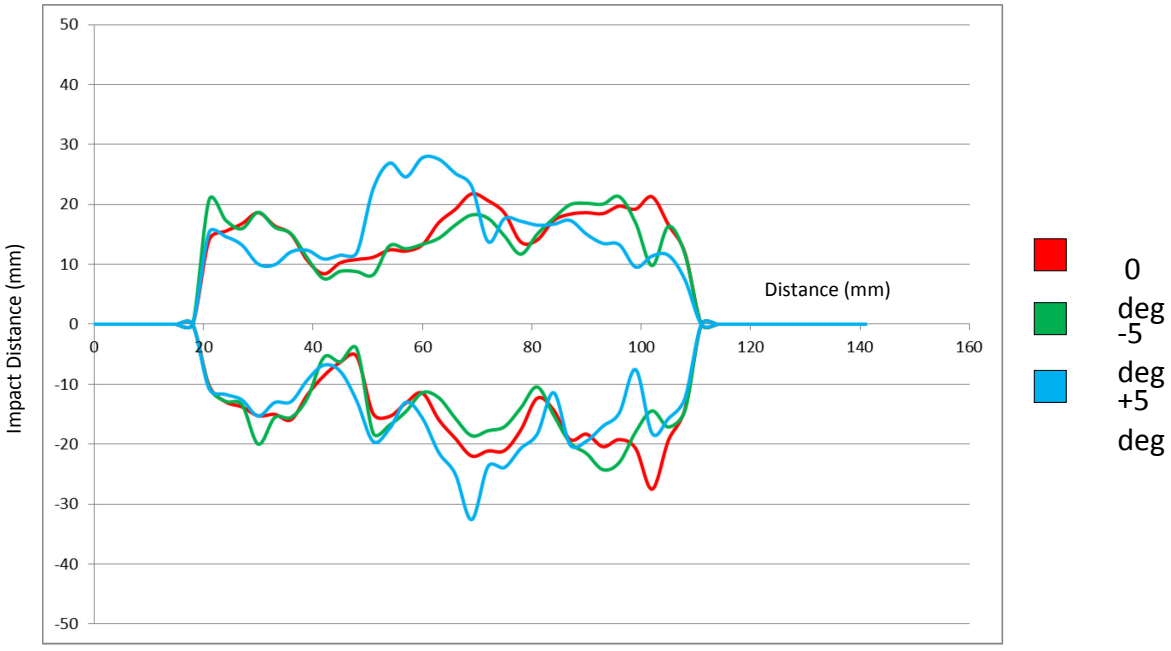

Figure 17 – Impact distance vs. distance (in mm) along 66mm pedicle screw axis for tilt angles of 0, +5°, and -5°.

Efficacy of VAT

When compared to sequence optimization using the titanium rod phantom, a tilt angle of -5° was less effective at reducing metal artifact in the case of the pedicle screw. Additionally, a tilt angle of +5° caused less of an increase in artifact. It is possible that given the severity of geometric distortions and intensity artifacts in EPI imaging that VAT has an effect on in-plane artifact reduction, but that the technique's increased usefulness in the rod phantom has to do with specific geometry. Since the dark region

present inferior to the rod is an important factor in determining the impact radius, the signal gradient introduced by VAT may compensate for the decreased intensity, resulting in increased homogeneity and causing the impact estimation algorithm to converge sooner. Unfortunately, this effect is geometry dependent and will not necessarily give good results in all situations.

While VAT has shown some improvement in metal artifact reduction in the iFOV sequence used, the reductions are on the order of 5-10%, and only a matter of tenths of millimeters. Given the severity of metal artifact in the iFOV sequence, these improvements are ultimately of little consequence and do not provide a meaningful increase in the region which can be effectively imaged.

CHAPTER 4

SPINE PHANTOM IMAGING AND CONCLUSIONS

Spine Phantom

Construction and Structural Imaging

In an attempt to simulate in-vivo imaging of an implanted spinal cord, a cervical spine phantom was constructed. The phantom was constructed using a cervical spine model comprising C1-C7 vertebrae purchased from 3B Scientific and two titanium pedicle screws obtained from Shriners Hospital. Because it was necessary to be able to measure diffusion based on the DTI data, a stalk of asparagus was used as a surrogate for the spinal cord due to its anisotropic diffusion properties.

The pedicle screws were implanted in the C5 vertebrae to simulate positioning as a result of surgical implantation. The screws were implanted from the anterior of the vertebrae and through the pedicle on either side of the spinal canal as they would be in a spinal stabilization application. As with other phantoms, the completed structure was suspended in a 2% agar gel for imaging. Figure 18 shows a three plane reconstruction of the phantom from axial images acquired with a turbo-SE T2 sequence, and Figure 19 shows pedicle screw location from a sagittal perspective. It is also important to note that the midline of the spinal cord is visible without artifact in the sagittal reconstruction in Figure 18.

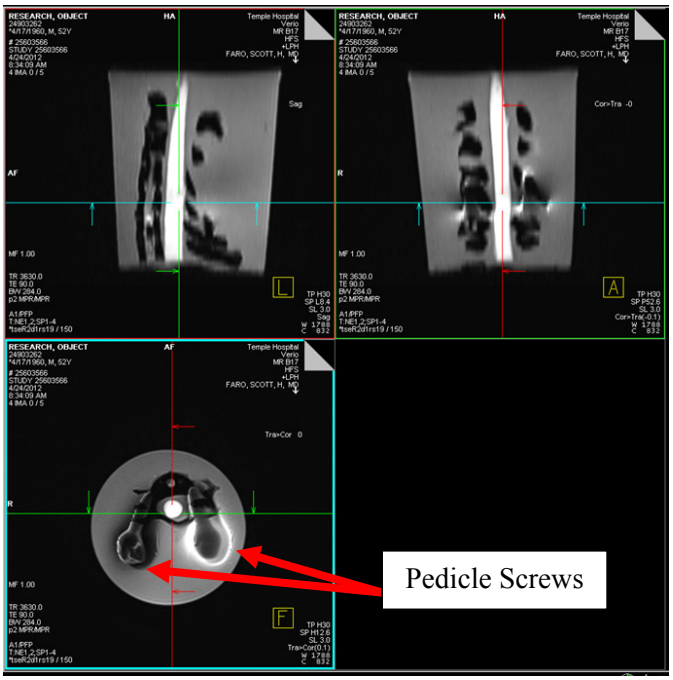

Figure 18 – Three plane view of cervical spine phantom. Pedicle screws are visible in the axial view (lower left).

Figure 19 – Sagittal view of spine phantom showing pedicle screw implantation at C5 vertebrae.

Diffusion Imaging

The spine phantom was imaged using the base iFOV sequence employed in the previously imaged phantoms (TE = 89ms, TR = 6600ms, voxel size = 1.2x1.2x3mm^3, b = 1000 s/mm^2, 20 diffusion directions, 2 averages). Images acquired away from the pedicle screws were good quality, and the anisotropic asparagus stalk was easily visible in color FA maps (Figure 20).

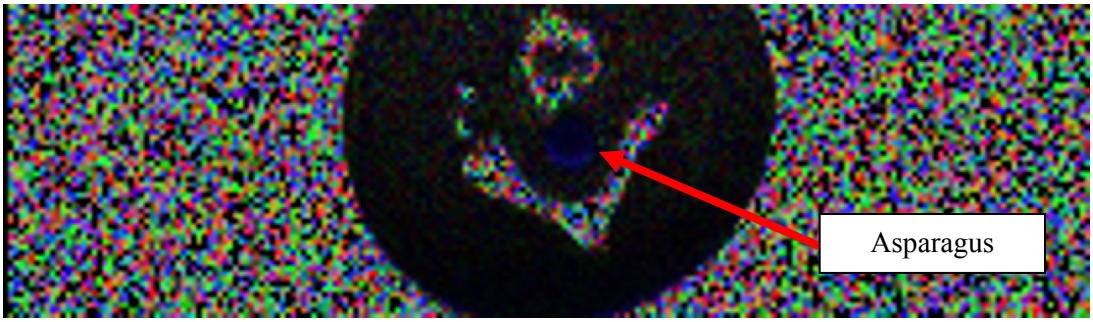

Figure 20 – Color FA map from axial slice of cervical spine phantom. The anisotropic asparagus stalk (blue) is clearly visible in the phantom's center.

As expected, distortions were severe near the metal implants, and diffusion measurements were impossible as the cord was not visible. Diffusion measurements were made on each slice where the cord was clearly visible. FA values ranged from 0.10 to 0.21, and decreased from superior to inferior, conveniently mimicking anisotropy in the spinal cord, and diffusivity measurements increased steadily from inferior to superior (Figure 21). The pedicle screws were centered at slice 19, and diffusion measurements were possible until slice 11, and could be resumed at slice 24. At a slice thickness of 3mm, this translates to diffusion measurement capability at a distance of 15mm superior to the pedicle screw center, and 24mm inferior to the screw center.

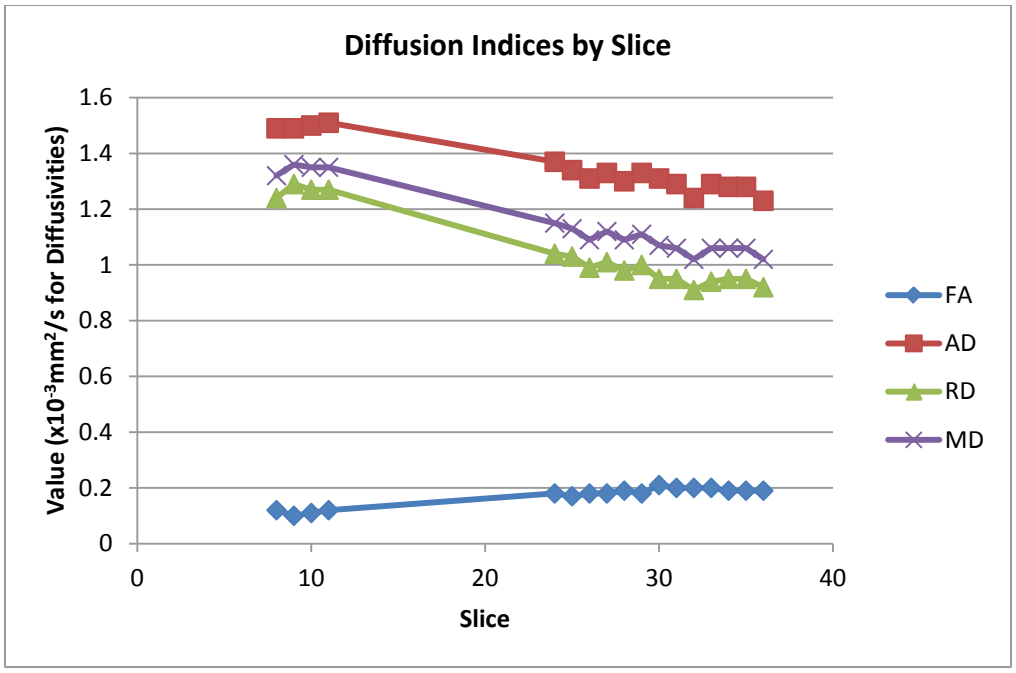

Figure 21 – Diffusion indices by slice for cervical spine phantom with pedicle screw implants. Markers represent measured values, lines with no marker present cover slices where measurement was not possible.

Conclusions

The results of this study suggest that diffusion imaging in the presence of metal implants, while difficult, is not without some utility. The results of the metal rod phantom imaging demonstrate that diffusion measurements may be practical at distances of 10mm from the center of a metal implant or even closer. It was demonstrated that this is true for smaller objects with simple, consistent geometry, i.e. minimal metal/tissue interfaces. These results show that patients with very minor metal instrumentation present should be considered as candidates for DTI, albeit evaluated on a case-by-case basis for implant size, orientation, and proximity to the spinal canal.

Additionally, even in subjects with greater instrumentation it may be possible to collect meaningful DTI data. Differences have been shown in FA and other DTI indices

superior and inferior to the actual site of injury between typically developing subjects and those with SCI(34). When imaging the spine phantom, DTI images were successfully acquired 15mm superior and 24mm inferior to the site of the metal implants. If knowledge of FA and diffusivity changes superior or inferior to the injury site is found to be diagnostic or prognostic in evaluation of subjects with SCI, then it may be valuable to collect DTI data in heavily implanted subjects even if data at the exact injury site is not obtainable. When using the current iFoV sequence, it will remain important to minimize potential heating effects and it may be necessary to limit the number of slices acquired to accomplish this.

One limitation of this study was the lack of a calibrated diffusion phantom. When imaging the spinal phantom, it was important to have a stand in for the spinal cord with at least some anisotropic diffusion characteristics so as to be able to differentiate the cord from the surrounding gel medium in DTI images and take measurements of diffusion indices. Asparagus served as a convenient and effective anisotropic diffusion phantom, but repeated measurements could not be used to verify or compare data because the consistency of the diffusion characteristics of the asparagus could not be assumed to remain identical over time or after placement in a new phantom. A calibrated phantom would have allowed for further verification of the accuracy of diffusion measurements made in the presence of metal implants.

The greatest limitation present was the nature of the iFoV diffusion sequence used. Because the iFoV sequence uses an echo-planar readout, it has an inherent susceptibility to metal artifact far greater than conventional spin-echo based sequences due to the reduced effective pixel bandwidth. Echo-planar sequences can exhibit

considerable geometric distortions at even relatively low magnetic susceptibility differences such as those found at air-tissue tissue interfaces, and susceptibility differences between tissue and titanium are an order of magnitude greater (178ppm vs. ~10ppm). The geometric distortions, signal voids, and intensity artifacts were somewhat manageable in the presence of surgical rods due to their small diameter and consistent geometry, but these issues were severe in the presence of the other surgical implants and in the spine phantom. While some small improvement was observable using available metal artifact reduction techniques (FoV size, VAT), the artifact severity far outpaced any compensation techniques.

After DTI was performed on the spine phantom, a TSE sequence with VAT and SEMAC implemented was used to image the phantom and examine the reduction in artifact. Considerable reduction in metal artifact was achieved using the VAT/SEMAC sequence without diffusion weighting (Figure 22). Also, acquisition direction is an important consideration when imaging. When scanning using a conventional TSE sequence, as previously mentioned, the midline of the spinal cord was clearly visible in the sagittal reconstruction using a standard TSE sequence, suggesting that a high resolution axial scan reformatted to sagittal may be preferable for avoiding metal artifacts when a sagittal image is desired for viewing.

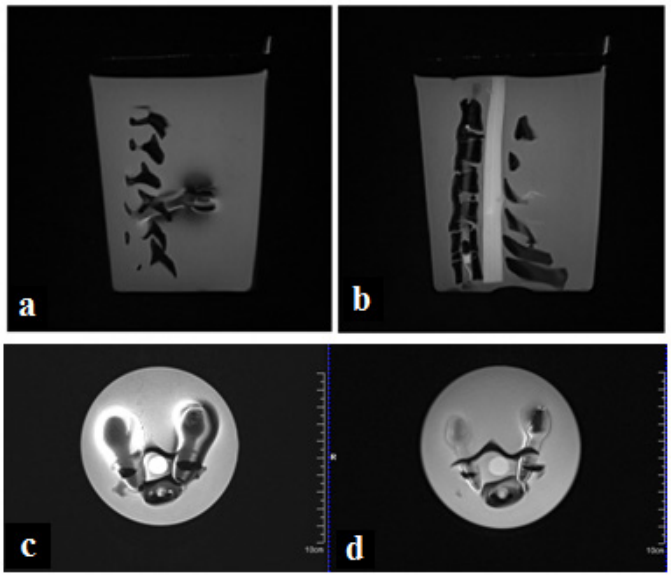

Figure 22 – Sagittal SEMAC image showing pedicle screw location (a) and midline of SC free of through-plane artifact (b). Conventional TSE T2 weighted image (c) and TSE T2 weighted scan using VAT and SEMAC (d). Reduction in in-plane artifact is clearly visible between the two scans.

The iFoV sequence used in this study has been shown to be very effective in acquiring DTI data for the spinal cord. However, while DTI of the spinal cord is possible in some cases in the presence of metal implants using the iFoV sequence employed in this study, the applications remain limited. Solving the challenge of imaging subjects with metal instrumentation and thus removing one of the most significant obstacles in the use of DTI as a diagnostic/prognostic tool in the evaluation and treatment of spinal cord injury will be important work for the crucial to the continued work with DTI of the spinal cord, and will have value to other fields, such as orthopaedics, as well. This work has sought to identify and characterize artifacts involved in DTI near metal implements by developing phantoms as well as new analysis techniques and software. By better understanding these artifacts and challenges, it is possible to more effectively develop novel techniques to allow imaging near metal in DTI.

REFERENCES

1. Basser PJ, Mattiello J & LeBihan D. MR diffusion tensor spectroscopy and imaging. Biophys J 1994:66:259-267.

2. Basser PJ, Mattiello J & Lebihan D. Estimation of the Effective Self-Diffusion Tensor from the NMR Spin Echo. Journal of Magnetic Resonance, Series B 1994:103:247-254.

3. McRobbie DW, Moore EA, Graves MJ & Prince MJ. MRI From Picture to Proton, 2nd edition. Cambridge University Press: New York: 2007. 394 p.

4. Stejskal E. Spin Diffusion Measurements: Spin Echoes in the Presence of a Time Dependent Field Gradient. J Chem Phys 1965:42:288-5.

5. Mattiello J, Basser PJ & Le Bihan D. The b matrix in diffusion tensor echo-planar imaging. Magnetic Resonance in Medicine 1997:37:292-300.

6. Jones DK. Gaussian Modeling of the Diffusion Signal. In: Johansen-Berg H and Behrens TEJ, editors. Diffusion MRI, 1st edition. Academic Press: London: 2009. 37-52 p.

7. Werring DJ, Clark CA, Barker GJ, Thompson AJ & Miller DH. Diffusion tensor imaging of lesions and normal-appearing white matter in multiple sclerosis. Neurology 1999:52:1626-1626.

8. Doran M, Hajnal JV, Bruggen NV, King MD, Young IR & Bydder GM. Normal and Abnormal White Matter Tracts Shown by MR Imaging using Directional Diffusion Weighted Sequences. J Comput Assist Tomogr 1990:14:865-873.

9. Pierpaoli C, Barnett A, Pajevic S, et al. Water Diffusion Changes in Wallerian Degeneration and Their Dependence on White Matter Architecture. Neuroimage 2001:13:1174-1185.

10. Cohen-Adad J, El Mendili MM, Lehericy S, et al. Demyelination and degeneration in the injured human spinal cord detected with diffusion and magnetization transfer MRI. Neuroimage 2011:55:1024-1033.

11. Finsterbusch J. High-resolution diffusion tensor imaging with inner field-of-view EPI. J Magn Reson Imaging 2009:29:987-993.

12. Finsterbusch J, Eippert F & Büchel C. Single, slice-specific z-shim gradient pulses improve T2*-weighted imaging of the spinal cord. Neuroimage .

13. Kharbanda HS, Alsop DC, Anderson AW, Filardo G & Hackney DB. Effects of cord motion on diffusion imaging of the spinal cord. Magn Reson Med 2006:56:334-339.

14. Laun F, Stieltjes B, Schluter M, Rupp R & Schad LR. Reproducible evaluation of spinal cord DTI using an optimized inner volume sequence in combination with probabilistic ROI analysis. Z Med Phys 2009:19:11-20.

15. Santarelli X, Garbin G, Ukmar M & Longo R. Dependence of the fractional anisotropy in cervical spine from the number of diffusion gradients, repeated acquisition and voxel size. Magn Reson Imaging 2010:28:70-76.

16. Barakat N, Mohamed FB, Shah P, et al. Diffusion Tensor Imaging of the Normal Pediatric Spinal Cord using an inner-FoV EPI Sequence. AJNR 2012:In Press.

17. Giove F, Garreffa G, Giulietti G, Mangia S, Colonnese C & Maraviglia B. Issues about the fMRI of the human spinal cord. Magn Reson Imaging 2004:22:1505-1516.

18. Schroth G & Klose U. Cerebrospinal fluid flow I. Physiology of cardiac-related pulsation.
. Neuroradiology 1992:35:1-9.

19. Schroth G & Klose U. Cerebrospinal fluid flow. II. Physiology of respiration-related pulsations. Neuroradiology 1992:35:10-15.

20. Barakat N, Middleton DM, Hunter L, et al. An Investigation of Motion Correction Algorithms for Pediatric Spinal Cord DTI in Normals and Patients with SCI. ISMRM Montreal 2011:6282.

21. Mansfield P. Multi-planar image formation using NMR spin echoes. J Phys C: Solid State Phys 1977:10:L55-L58.

22. Schenck JF. The role of magnetic susceptibility in magnetic resonance imaging: MRI magnetic compatibility of the first and second kinds. Med Phys 1996:23:815-850.

23. Lüdeke KM, Röschmann P & Tischler R. Susceptibility artefacts in NMR imaging. Magn Reson Imaging 1985:3:329-343.

24. Boesch C, Gruetter R & Martin E. Temporal and spatial analysis of fields generated by eddy currents in superconducting magnets: Optimization of corrections and quantitative characterization of magnet/gradient systems. Magnetic Resonance in Medicine 1991:20:268-284.

25. Ahn CB & Cho ZH. Analysis of the eddy-current induced artifacts and the temporal compensation in nuclear magnetic resonance imaging. Medical Imaging, IEEE Transactions on 1991:10:47-52.

26. Macovski A & Conolly S. Novel approaches to low-cost MRI. Magnetic Resonance in Medicine 1993:30:221-230.

27. Venook RD, Matter NI, Ramachandran M, et al. Prepolarized magnetic resonance imaging around metal orthopedic implants. Magnetic Resonance in Medicine 2006:56:177-186.

28. Cho ZH, Kim DJ & Kim YK. Total inhomogeneity correction including chemical shifts and susceptibility by view angle tilting. Med Phys 1988:15.

29. Chang SD, Lee MJ, Munk PL, Janzen DL, MacKay A & Xiang Q. MRI of spinal hardware: comparison of conventional T1-weighted sequence with a new metal artifact reduction sequence. Skeletal Radiol 2001:30:213-218.

30. Lu W, Pauly KB, Gold GE, Pauly JM & Hargreaves BA. SEMAC: Slice encoding for metal artifact correction in MRI. Magnetic Resonance in Medicine 2009:62:66-76.

31. Hargreaves BA, Chen W, Lu W, et al. Accelerated slice encoding for metal artifact correction. Journal of Magnetic Resonance Imaging 2010:31:987-996.

32. Chen CA, Chen W, Goodman SB, et al. New MR imaging methods for metallic implants in the knee: Artifact correction and clinical impact. Journal of Magnetic Resonance Imaging 2011:33:1121-1127.

33. Petersilge CA, Lewin JS, Duerk JL, Yoo JU & Ghaneyem AJ. Optimizing imaging parameters for MR evaluation of the spine with titanium pedicle screws. American Journal of Roentgenology 1996:166:1213-1218.

34. Mohamed FB, Hunter LN, Barakat N, et al. Diffusion Tensor Imaging of the Pediatric Spinal Cord at 1.5T: Preliminary Results. American Journal of Neuroradiology 2011:32:339-345.

APPENDIX A

SURGICAL ROD MEASUREMENTS

Table 8 – Homogeneous region measurements for surgical rods.

	Slice	Mean Intensity	Stdv.	Stdv/Mean
	25	261	34	0.130
	26	255	33	0.129
Ti 5.5mm	27	258	31	0.120
iFoV	28	252	31	0.123
	29	257	30	0.117
	25	395	30	0.076
	26	390	33	0.085
Ti 5.5mm	27	399	32	0.080
full FoV	28	392	33	0.084
	29	400	34	0.085
	25	274	32	0.117
	26	264	32	0.121
Ti 3.5mm	27	273	32	0.117
iFoV	28	266	30	0.113
	29	272	32	0.118
	25	416	32	0.077
	26	410	34	0.083
Ti 3.5mm	27	415	35	0.084
full FoV	28	411	36	0.088
	29	415	38	0.092
	22	266	33	0.124
	23	273	30	0.110
CoCr 5.5mm	24	266	30	0.113
iFoV	25	272	29	0.107
	26	267	30	0.112
	22	401	44	0.110
	23	404	45	0.111
CoCr 5.5mm	24	401	45	0.112
full FoV	25	407	52	0.128
	26	404	55	0.136

Table 9 – Impact radius measurements for surgical rods.

	Slice	Impact Radius (mm)	Std. Dev. Tolerance Criteria
	25	7.2	0.15
	26	8.1	0.15
Ti 5.5mm	27	8.4	0.15
iFoV	28	8.1	0.15
	29	6.9	0.15
	25	6.9	0.10
	26	7.2	0.10
Ti 5.5mm	27	7.2	0.10
full FoV	28	6.3	0.10
	29	6.9	0.10
	25	5.4	0.15
	26	5.7	0.15
Ti 3.5mm	27	5.1	0.15
iFoV	28	5.4	0.15
	29	5.7	0.15
	25	6.3	0.10
	26	6.6	0.10
Ti 3.5mm	27	6.3	0.10
full FoV	28	6.6	0.10
	29	6	0.10
	22	9	0.15
	23	7.2	0.15
CoCr 5.5mm	24	7.2	0.15
iFoV	25	6.6	0.15
	26	9.3	0.15
	22	8.7	0.19
	23	7.5	0.18
CoCr 5.5mm	24	6.9	0.18
full FoV	25	8.1	0.18
	26	6	0.21

APPENDIX B

SURGICAL IMPLEMENT MEASUREMENTS

Table 10 – Impact distance measurements for 66mm screw, axial orientation.

	Distance from center line (mm)			Distance from center line (mm)	
Slice	**Left**	**Right**	**Slice**	**Left**	**Right**
1	0.0	0.0	25	-21.1	20.6
2	0.0	0.0	26	-21.1	18.6
3	0.0	0.0	27	-17.6	13.7
4	0.0	0.0	28	-12.3	14.1
5	0.0	0.0	29	-14.3	17.3
6	0.0	0.0	30	-19.2	18.4
7	0.0	0.0	31	-18.3	18.6
8	-10.2	14.1	32	-20.4	18.5
9	-12.9	15.5	33	-19.2	19.7
10	-13.8	16.8	34	-20.7	19.2
11	-15.3	18.6	35	-27.5	21.3
12	-15.0	16.4	36	-19.3	16.6
13	-15.9	15.0	37	-14.2	11.9
14	-11.7	10.6	38	0.0	0.0
15	-8.6	8.4	39	0.0	0.0
16	-6.3	10.3	40	0.0	0.0
17	-5.4	10.8	41	0.0	0.0
18	-14.9	11.2	42	0.0	0.0
19	-15.4	12.4	43	0.0	0.0
20	-13.1	12.2	44	0.0	0.0
21	-11.5	13.3	45	0.0	0.0
22	-15.9	17.0	46	0.0	0.0
23	-19.0	19.2	47	0.0	0.0
24	-22.0	21.8	48	0.0	0.0

Table 11 – Impact distance measurements for 43mm screw, sagittal orientation.

	Distance from center line (mm)			Distance from center line (mm)	
Slice	**Left**	**Right**	**Slice**	**Left**	**Right**
1	0.0	0.0	25	-31.8	36.0
2	0.0	0.0	26	-28.0	28.5
3	0.0	0.0	27	-27.8	24.2
4	0.0	0.0	28	-30.8	28.4
5	0.0	0.0	29	-29.7	27.9
6	0.0	0.0	30	-26.1	29.6
7	0.0	0.0	31	-26.0	22.9
8	0.0	0.0	32	-16.0	21.5
9	0.0	0.0	33	-25.3	25.7
10	0.0	0.0	34	-13.4	18.1
11	0.0	0.0	35	-19.8	22.9
12	0.0	0.0	36	-14.1	19.9
13	0.0	0.0	37	-11.2	8.6
14	-24.3	21.9	38	0.0	0.0
15	-26.0	29.4	39	0.0	0.0
16	-27.1	24.6	40	0.0	0.0
17	-26.5	27.9	41	0.0	0.0
18	-29.1	30.3	42	0.0	0.0
19	-26.9	26.0	43	0.0	0.0
20	-26.5	24.3	44	0.0	0.0
21	-25.0	26.0	45	0.0	0.0
22	-31.3	27.8	46	0.0	0.0
23	-35.0	30.2	47	0.0	0.0
24	-35.3	31.2	48	0.0	0.0

Table 12 – Impact distance measurements for titanium cage, axial orientation.

	Distance from center line (mm)			Distance from center line (mm)	
Slice	**Left**	**Right**	**Slice**	**Left**	**Right**
1	0.0	0.0	25	-11.9	11.0
2	0.0	0.0	26	-9.6	8.8
3	0.0	0.0	27	0.0	0.0
4	0.0	0.0	28	0.0	0.0
5	-10.0	12.4	29	0.0	0.0
6	-12.5	16.0	30	0.0	0.0
7	-13.0	14.4	31	0.0	0.0
8	-11.6	13.2	32	0.0	0.0
9	-10.7	12.1	33	0.0	0.0
10	-10.4	11.9	34	0.0	0.0
11	-10.5	13.4	35	0.0	0.0
12	-9.9	13.9	36	0.0	0.0
13	-11.4	13.5	37	0.0	0.0
14	-9.9	12.7	38	0.0	0.0
15	-11.6	11.6	39	0.0	0.0
16	-12.4	10.1	40	0.0	0.0
17	-18.0	10.7	41	0.0	0.0
18	-12.4	11.6	42	0.0	0.0
19	-12.4	9.0	43	0.0	0.0
20	-11.2	9.2	44	0.0	0.0
21	-14.5	12.7	45	0.0	0.0
22	-15.2	13.5	46	0.0	0.0
23	-15.0	14.0	47	0.0	0.0
24	-14.0	12.8	48	0.0	0.0

Table 13 – Impact distance measurements for 66mm screw, axial, -5° tilt angle.

	Distance from center line (mm)			Distance from center line (mm)	
Slice	**Left**	**Right**	**Slice**	**Left**	**Right**
1	0.0	0.0	25	-17.7	17.7
2	0.0	0.0	26	-17.1	14.8
3	0.0	0.0	27	-13.9	11.7
4	0.0	0.0	28	-10.4	15.1
5	0.0	0.0	29	-15.1	17.7
6	0.0	0.0	30	-19.7	20.0
7	0.0	0.0	31	-21.5	20.2
8	-10.4	20.8	32	-24.2	20.1
9	-12.8	17.4	33	-23.0	21.3
10	-13.4	16.0	34	-17.9	16.9
11	-20.0	18.7	35	-14.4	9.8
12	-15.5	16.2	36	-17.1	16.4
13	-15.5	15.1	37	-14.4	11.7
14	-12.2	11.0	38	0.0	0.0
15	-5.5	7.6	39	0.0	0.0
16	-6.2	8.9	40	0.0	0.0
17	-4.1	8.8	41	0.0	0.0
18	-18.1	8.3	42	0.0	0.0
19	-16.8	13.1	43	0.0	0.0
20	-14.5	12.6	44	0.0	0.0
21	-11.4	13.4	45	0.0	0.0
22	-12.2	14.4	46	0.0	0.0
23	-15.6	16.6	47	0.0	0.0
24	-18.6	18.3	48	0.0	0.0

Table 14 – Impact distance measurements for 66mm screw, axial, +5° tilt angle.

	Distance from center line (mm)			Distance from center line (mm)	
Slice	**Left**	**Right**	**Slice**	**Left**	**Right**
1	0.0	0.0	25	-23.7	13.8
2	0.0	0.0	26	-23.9	17.6
3	0.0	0.0	27	-20.7	17.2
4	0.0	0.0	28	-18.3	16.5
5	0.0	0.0	29	-11.4	16.7
6	0.0	0.0	30	-20.1	17.3
7	0.0	0.0	31	-19.5	15.0
8	-10.8	15.3	32	-17.0	13.5
9	-11.7	14.6	33	-14.8	13.3
10	-12.6	13.2	34	-7.6	9.5
11	-15.3	10.0	35	-18.2	11.4
12	-13.1	9.9	36	-15.7	11.5
13	-12.9	12.1	37	-12.4	7.4
14	-9.3	12.3	38	0.0	0.0
15	-6.8	10.9	39	0.0	0.0
16	-7.9	11.5	40	0.0	0.0
17	-12.8	11.9	41	0.0	0.0
18	-19.6	22.6	42	0.0	0.0
19	-17.4	26.9	43	0.0	0.0
20	-13.0	24.6	44	0.0	0.0
21	-15.7	27.8	45	0.0	0.0
22	-21.4	27.5	46	0.0	0.0
23	-25.0	25.2	47	0.0	0.0
24	-32.6	23.0	48	0.0	0.0